Ultrafast nonlinear optical studies of silicon nanowaveguides

Ali R. Motamedi,[1,*] Amir H. Nejadmalayeri,[1] Anatol Khilo,[1] Franz X. Kärtner,[1,2] and Erich P. Ippen[1]

[1]*Research Laboratory of Electronics, and Department of Electrical Engineering and Computer Science, Massachusetts Institute of Technology, 77 Massachusetts Avenue, Cambridge, Massachusetts 02139, USA*
[2]*Center for Free-Electron Laser Science, DESY, and Department of Physics, University of Hamburg, Notkestraße 85, 22607 Hamburg, Germany*
[*]*motamedi@alum.mit.edu*

Abstract: Results of a self-consistent ultrafast study of nonlinear optical properties of silicon nanowaveguides using heterodyne pump-probe technique are reported. The two-photon absorption coefficient and free-carrier absorption effective cross-section were determined to be 0.68cm/GW, and 1.9×10^{-17} cm^2, respectively and the Kerr coefficient and free-carrier-induced refractive index change 0.32×10^{-13} cm^2/W, and -5.5×10^{-21} cm^3, respectively. The effects of the proton bombardment on the linear loss and the carrier lifetime of the devices were also studied. Carrier lifetime reduction from 330ps to 33ps with a linear loss of only 14.8dB/cm was achieved using a proton bombardment level of 10^{15}/cm^2.

©2012 Optical Society of America

References and links

1. D. Englund, H. Altug, B. Ellis, and J. Vučković, "Ultrafast photonic crystal lasers," Laser Photon. Rev. **2**(4), 264–274 (2008).
2. N. Fujioka, T. Chu, and M. Ishizaka, "Compact and low power consumption hybrid integrated wavelength tunable laser module using silicon waveguide resonators," J. Lightwave Technol. **28**, 3115–3120 (2010).
3. H. Ji, M. Galili, H. Hu, M. H. Pu, L. K. Oxenlowe, K. Yvind, J. M. Hvam, and P. Jeppesen, "1.28-Tb/s demultiplexing of an OTDM DPSK data signal using a silicon waveguide," IEEE Photon. Technol. Lett. **22**(23), 1762–1764 (2010).
4. G. L. Li, X. Z. Zheng, J. Lexau, Y. Luo, H. Thacker, T. Pinguet, P. Dong, D. Z. Feng, S. R. Liao, R. Shafiiha, M. Asghari, J. Yao, J. Shi, I. N. Shubin, D. Patil, F. Liu, K. Raj, R. Ho, J. E. Cunningham, and A. V. Krishnamoorthy, "Ultralow-power silicon photonic interconnect for high-performance computing systems," Optoelectronic Interconnects and Component Integration IX **7607**, 760703 (2010).
5. B. Jalali and S. Fathpour, "Silicon photonics," J. Lightwave Technol. **24**(12), 4600–4615 (2006).
6. B. Jalali, "Silicon photonics nonlinear optics in the mid-infrared," Nat. Photonics **4**(8), 506–508 (2010).
7. M. Hochberg and T. Baehr-Jones, "Towards fabless silicon photonics," Nat. Photonics **4**(8), 492–494 (2010).
8. R. A. Soref and B. R. Bennett, "Electrooptical effects in silicon," IEEE J. Quantum Electron. **23**(1), 123–129 (1987).
9. H. K. Tsang and Y. Liu, "Nonlinear optical properties of silicon waveguides," Semicond. Sci. Technol. **23**(6), 064007 (2008).
10. F. X. Kärtner, S. Akiyama, G. Barbastathis, T. Barwicz, H. Byun, D. T. Danielson, F. Gan, F. Grawert, C. W. Holzwarth, J. L. Hoyt, E. P. Ippen, M. Kim, L. C. Kimerling, J. Liu, J. Michel, O. O. Olubuyide, J. S. Orcutt, M. Park, M. Perrott, M. A. Popovic, P. T. Rackich, R. J. Ram, H. I. Smith, and M. R. Watts, "Electronic photonic integrated circuits for high speed, high resolution, analog to digital conversion," Proc. SPIE **6125**, 612503, 612503-14 (2006).
11. A. Alduino, L. Liao, R. Jones, M. Morse, B. Kim, W.-Z. Lo, J. Basak, B. Koch, H.-F. Liu, H. Rong, M. Sysak, C. Krause, R. Saba, D. Lazar, L. Horwitz, R. Bar, S. Litski, A. Liu, K. Sullivan, O. Dosunmu, N. Na, T. Yin, F. Haubensack, I. W. Hsieh, J. Heck, R. Beatty, H. Park, J. Bovington, S. Lee, H. Nguyen, H. Au, K. Nguyen, P. Merani, M. Hakami, and M. Paniccia, "Demonstration of a high speed 4-channel integrated silicon photonics WDM link with hybrid silicon lasers," in *Integrated Photonics Research, Silicon and Nanophotonics*, (Optical Society of America, 2010), paper PDIWI5 (2010).
12. D. A. B. Miller, "Optical interconnects to electronic chips," Appl. Opt. **49**(25), F59–F70 (2010).
13. M. Khorasaninejad and S. S. Saini, "All-optical logic gates using nonlinear effects in silicon-on-insulator waveguides," Appl. Opt. **48**(25), F31–F37 (2009).

14. J. Y. Lee, L. H. Yin, G. P. Agrawal, and P. M. Fauchet, "Ultrafast optical switching based on nonlinear polarization rotation in silicon waveguides," Opt. Express **18**(11), 11514–11523 (2010).
15. A. Martínez, J. Blasco, P. Sanchis, J. V. Galán, J. García-Rupérez, E. Jordana, P. Gautier, Y. Lebour, S. Hernández, R. Spano, R. Guider, N. Daldosso, B. Garrido, J. M. Fedeli, L. Pavesi, and J. Martí, "Ultrafast all-optical switching in a silicon-nanocrystal-based silicon slot waveguide at telecom wavelengths," Nano Lett. **10**(4), 1506–1511 (2010).
16. Y. H. Kuo, H. Rong, V. Sih, S. Xu, M. Paniccia, and O. Cohen, "Demonstration of wavelength conversion at 40 Gb/s data rate in silicon waveguides," Opt. Express **14**(24), 11721–11726 (2006).
17. Q. F. Xu and M. Lipson, "All-optical logic based on silicon micro-ring resonators," Opt. Express **15**(3), 924–929 (2007).
18. P. W. Juodawlkis, J. C. Twichell, G. E. Betts, J. J. Hargreaves, R. D. Younger, J. L. Wasserman, F. J. O'Donnell, K. G. Ray, and R. C. Williamson, "Optically sampled analog-to-digital converters," IEEE Trans. Microw. Theory Tech. **49**(10), 1840–1853 (2001).
19. G. C. Valley, "Photonic analog-to-digital converters," Opt. Express **15**(5), 1955–1982 (2007).
20. F. X. Kartner, R. Amatya, M. Araghchini, J. Birge, H. Byun, J. Chen, M. Dahlem, N. A. DiLello, F. Gan, C. W. Holzwarth, J. L. Hoyt, E. P. Ippen, A. Khilo, J. Kim, M. Kim, A. Motamedi, J. S. Orcutt, M. Park, M. Perrott, M. A. Popovi, R. J. Ram, H. I. Smith, G. R. Zhou, S. J. Spector, T. M. Lyszczarz, M. W. Geis, D. M. Lennon, J. U. Yoon, M. E. Grein, and R. T. Schulein, "Photonic analog-to-digital conversion with electronic-photonic integrated circuits," Proc. SPIE **6898**, 689806, 689806-15 (2008).
21. A. H. Nejadmalayeri, M. Grein, A. Khilo, J. P. Wang, M. Y. Sander, M. Peng, C. M. Sorace, E. P. Ippen, and F. X. Kärtner, "A 16-fs aperture-jitter photonic ADC: 7.0 ENOB at 40 GHz," in *Lasers and Electro-Optics (CLEO)*, CHTI6 (2011).
22. M. E. Grein, S. J. Spector, A. Khilo, A. H. Najadmalayeri, M. Y. Sander, M. Peng, J. Wang, C. M. Sorace, M. W. Geis, M. M. Willis, D. M. Lennon, T. M. Lyszczarz, E. P. Ippen, and F. X. Kärtner, "Demonstration of a 10 GHz CMOS-compatible integrated photonic analog-to-digital converter," in *Lasers and Electro-Optics (CLEO)*, CHTI1 (2011).
23. M. A. Popovic, T. Barwicz, M. S. Dahlem, F. W. Gan, C. W. Holzwarth, P. T. Rakich, M. R. Watts, H. I. Smith, F. X. Kärtner, and E. P. Ippen, "Hitless-reconfigurable and bandwidth-scalable silicon photonic circuits for telecom and interconnect applications," in *2008 Conference on Optical Fiber Communication/National Fiber Optic Engineers Conference*, 2296–2298 (2008).
24. J. S. Orcutt, A. Khilo, M. A. Popovic, C. W. Holzwarth, H. Li, J. Sun, B. Moss, M. S. Dahlem, E. P. Ippen, J. L. Hoyt, V. Stojanovic, F. X. Kärtner, H. I. Smith, and R. J. Ram, "Photonic integration in a commercial scaled bulk-CMOS process," in *International Conference on Photonics in Switching 2009*, 170–171 (2009).
25. C. W. Holzwarth, A. Khilo, M. Dahlem, M. A. Popovic, F. X. Kärtner, E. P. Ippen, and H. I. Smith, "Device architecture and precision nanofabrication of microring-resonator filter banks for integrated photonic systems," J. Nanosci. Nanotechnol. **10**(3), 2044–2052 (2010).
26. A. Khilo, M. A. Popović, M. Araghchini, and F. X. Kärtner, "Efficient planar fiber-to-chip coupler based on two-stage adiabatic evolution," Opt. Express **18**(15), 15790–15806 (2010).
27. C. R. Doerr, P. J. Winzer, Y.-K. Chen, S. Chandrasekhar, M. S. Rasras, L. Chen, T.-Y. Liow, K.-W. Ang, and G.-Q. Lo, "Monolithic polarization and phase diversity coherent receiver in silicon," J. Lightwave Technol. **28**(4), 520–525 (2010).
28. T. Barwicz, M. A. Popovi, F. Gan, M. S. Dahlem, C. W. Holzwarth, P. T. Rakich, E. P. Ippen, F. X. Kartner, and H. I. Smith, "Reconfigurable silicon photonic circuits for telecommunication applications," Proc. SPIE **6872**, 68720Z, 68720Z-12 (2008).
29. J. Leuthold, C. Koos, and W. Freude, "Nonlinear silicon photonics," Nat. Photonics **4**(8), 535–544 (2010).
30. Q. Lin, O. J. Painter, and G. P. Agrawal, "Nonlinear optical phenomena in silicon waveguides: modeling and applications," Opt. Express **15**(25), 16604–16644 (2007).
31. L. Liao, D. Samara-Rubio, M. Morse, A. Liu, D. Hodge, D. Rubin, U. Keil, and T. Franck, "High speed silicon Mach-Zehnder modulator," Opt. Express **13**(8), 3129–3135 (2005).
32. M. R. Watts, W. A. Zortman, D. C. Trotter, R. W. Young, and A. L. Lentine, "Low-voltage, compact, depletion-mode, silicon Mach-Zehnder modulator," IEEE J. Sel. Top. Quantum Electron. **16**(1), 159–164 (2010).
33. L. Yin, Q. Lin, and G. P. Agrawal, "Soliton fission and supercontinuum generation in silicon waveguides," Opt. Lett. **32**(4), 391–393 (2007).
34. K. L. Hall, G. Lenz, E. P. Ippen, and G. Raybon, "Heterodyne pump - probe technique for time-domain studies of optical nonlinearities in waveguides," Opt. Lett. **17**(12), 874–876 (1992).
35. A. C. Turner-Foster, M. A. Foster, J. S. Levy, C. B. Poitras, R. Salem, A. L. Gaeta, and M. Lipson, "Ultrashort free-carrier lifetime in low-loss silicon nanowaveguides," Opt. Express **18**(4), 3582–3591 (2010).
36. P. Apiratikul, A. M. Rossi, and T. E. Murphy, "Nonlinearities in porous silicon optical waveguides at 1550 nm," Opt. Express **17**(5), 3396–3406 (2009).
37. K. Preston, P. Dong, B. Schmidt, and M. Lipson, "High-speed all-optical modulation using polycrystalline silicon microring resonators," Appl. Phys. Lett. **92**(15), 151104 (2008).
38. P. G. Coleman, C. P. Burrows, and A. P. Knights, "Simple expression for vacancy concentrations at half ion range following MeV ion implantation of silicon," Appl. Phys. Lett. **80**(6), 947–949 (2002).
39. P. J. Foster, J. K. Doylend, P. Mascher, A. P. Knights, and P. G. Coleman, "Optical attenuation in defect-engineered silicon rib waveguides," J. Appl. Phys. **99**(7), 073101 (2006).
40. A. P. Knights and G. F. Hopper, "Effect of ion implantation induced defects on optical attenuation in silicon waveguides," Electron. Lett. **39**(23), 1648–1649 (2003).

41. D. Dimitropoulos, S. Fathpour, and B. Jalali, "Limitations of active carrier removal in silicon Raman amplifiers and lasers," Appl. Phys. Lett. **87**(26), 261108 (2005).
42. C. Koos, L. Jacome, C. Poulton, J. Leuthold, and W. Freude, "Nonlinear silicon-on-insulator waveguides for all-optical signal processing," Opt. Express **15**(10), 5976–5990 (2007).
43. M. Popovic, "Complex-frequency leaky mode computations using PML boundary layers for dielectric resonant structures," in OSA Trends in Optics and Photonics (Optical Society of America, 2003), ITuD4 (2003).
44. S. M. Sze and K. K. Ng, *Physics of Semiconductor Devices,* 3rd ed. (Wiley-Interscience, 2007).
45. N. M. Wright, D. J. Thomson, K. L. Litvinenko, W. R. Headley, A. J. Smith, A. P. Knights, F. Y. Gardes, G. Z. Mashanovich, R. Gwilliam, and G. T. Reed, "Free carrier lifetime modification for silicon waveguide based devices," in *Group IV Photonics, 2008 5th IEEE International Conference on*, 122–124 (2008).
46. J. K. Doylend, P. E. Jessop, and A. P. Knights, "Optical attenuation in ion-implanted silicon waveguide racetrack resonators," Opt. Express **19**(16), 14913–14918 (2011).
47. A. R. Motamedi, J. J. Plant, J. P. Donnelly, P. W. Juodawlkis, and E. P. Ippen, "Ultrafast nonlinearities and gain dynamics in high-power semiconductor amplifiers," Appl. Phys. Lett. **93**(25), 251106 (2008).

1. Introduction

Silicon-based optical devices have received a great deal of attention for potential application to high speed signal processing and on-chip communications [1–7]. Nonlinear optical properties of silicon were originally studied by Soref et al. [8], and have been subsequently characterized with various different techniques that have resulted in a large range of published data [9]. For this paper, we utilized the heterodyne femtosecond pump-probe technique to study the nonlinear index and absorption properties of silicon with high sensitivity and dynamic range and to investigate the ultrafast components and related longer recovery processes at the same time. Essential to the accuracy of these studies was careful characterization of the linear coupling and propagation losses.

Nonlinear optical properties of silicon have been utilized in the design of modulators, receivers, and filters in optical communication demonstrations with bit rates on the order of 1Tbits/sec [3] and real-time A-to-D converters with sampling rates of several tens of Gbits/sec [10]. A major advantage of silicon photonic devices is that they can be produced efficiently by taking advantage of the mature silicon processing technology that has been extensively developed to permit low-cost, large-volume electronic circuit production. This makes possible optical devices compatible with the CMOS technology for on-chip integration. The high bandwidths, high speeds and energy efficiency of optical communication circuits allow for on-board communication with performance greatly surpassing the electronic alternative [11, 12].

The small feature sizes that can be achieved in silicon fabrication allow for a miniaturization of devices that makes them suitable for on-chip integration. To realize on-board all-optical processing, it is necessary to design and implement both passive and active optical components based on silicon technology. Some of the inherent properties of silicon that facilitate the design and implementation of such components are nonlinear optical properties of silicon that can be utilized in the design of optical switches [13–15] and wavelength converters [16, 17], and play an important part in the performance of analog-to-digital converters [18–22]. As this technology is based on silicon-on-insulator (SOI) structures, a very high-index contrast (HIC) can be achieved between Si ($n = 3.45$) on SiO_2 ($n = 1.45$). This high index contrast makes possible highly-confined optical modes in the 1.5μm wavelength range and allows for on-chip features such as small-radius ring resonators, and tight, low-loss bends that are not easily achieved using other technologies [23]. Efficient, low-loss transmission of optical modes in waveguides with submicron features makes these devices suitable for the integration of optics and electronics on the same chip [23–28].

One of the main advantages of silicon photonic devices is their transparency in the 1.5μm telecom wavelength range in which the photon energy (0.8eV) is below the bandgap of silicon (1.12eV). For increasingly higher bit-rate optical signals, shorter pulses need to be transmitted in silicon waveguides while keeping the per-pulse energy of the optical signals constant. This leads to pulses with high peak powers which combined with the small feature sizes of devices can lead to intensities in the order of MW/cm^2. At such intensities, the nonlinear optical properties of silicon begin to impose limitations on the maximum data rate that can be carried by such devices. Therefore, they need to be accurately characterized.

To study the nonlinear optical properties of silicon, we can examine both the real and imaginary parts of the refractive index. The real and imaginary parts of the complex refractive index describe the processes contributing to the optical phase shift and loss of an optical signal propagating along the length of a waveguide, respectively. The imaginary part of the complex refractive-index demonstrates the loss mechanisms and is given by [29, 30]

$$n_I = \frac{\lambda}{4\pi}\left(\alpha_{lin} + \beta I + \sigma f_\alpha(N)\right), \tag{1}$$

where α_{lin} is the linear propagation loss, β is the two photon absorption coefficient, $\sigma f_\alpha(N)$ is the loss incurred due to the interaction of the optical field with the TPA-generated free-carriers of density, N, and I is the intensity of the optical field. Linear loss, α_{lin} is due to impurities of the constituent elements, and the surface roughness of the waveguides due to fabrication. The linear loss is independent of the optical power inside the waveguide and is relatively constant over the length of the device so that total loss scales linearly with the length.

Nonlinear optical losses are caused by two processes, two-photon absorption (TPA) and TPA-induced free-carrier absorption (FCA). The indirect bandgap of silicon is 1.12eV, and two photons at 1500nm with energy of approximately 0.8eV in combination with a phonon can excite an electron from the valence band to the conduction band, a process called two-photon absorption. The free-carriers that are excited to the conduction band can further absorb photons and be excited to higher energy states. This absorption process is named free-carrier absorption (FCA) and its magnitude is proportional to the density of free-carriers. TPA loss is an instantaneous process and is proportional to the optical intensity. FCA loss is caused by TPA-induced carriers, and its magnitude is proportional to the square of intensity integrated over time, and can persist with the lifetime of the induced free carriers.

The real part of the refractive index determines the amount of phase shift that an optical pulse incurs as it propagates through a silicon layer. This phase shift is exploited in the design of optical switches [14, 15], Mach-Zehnder interferometers [31, 32], super-continuum generation [33], and all-optical wavelength converters [10]. The real part of the complex refractive-index is given by [29, 30]:

$$n_R = n_0 + n_2 I + \xi f_\phi(N), \tag{2}$$

where n_0 is the refractive index of the waveguide, n_2 is the Kerr coefficient, $\xi f_\phi(N)$ is the induced phase due to the interaction of the optical field with the TPA-generated free carriers of density N, and I is the intensity of the optical field.

Measurement techniques employed to characterize the magnitude of the TPA coefficient have previously consisted of Z-scan technique, picosecond pump-probe, and fitting a model to the transmission response. Reported values vary between 0.44 to 0.9 cm/GW in the 1400-1600nm wavelength range [9]. Similarly, the optical Kerr coefficient has been characterized using Z-scan, self-phase modulation (SPM), and four-wave mixing (FWM) techniques in silicon waveguides. The extracted values of the Kerr coefficient range from 2.8×10^{-14} cm^2/W to 14.5×10^{-14} cm^2/W [9]. One of the factors contributing to the large variation in these numbers may be the accuracy of determining the optical power in a silicon device.

In this paper, we implement the linear cut-back technique combined with the nonlinear transfer function of a device to determine the input and output coupling losses as well as the linear internal loss, and thereby determining accurately the internal optical power. In addition, direct measurement of the nonlinear optical parameters in Eq. (1) and Eq. (2) reduces the uncertainty. For this reason, a heterodyne pump-probe experiment is utilized to simultaneously provide both magnitude and phase information [34]. In addition, the heterodyne pump-probe technique has the dynamic range and sensitivity to extract both the instantaneous responses and the longer lived FCA effects as a function of the carrier density.

TPA-induced free carrier effects are affected by the free-carrier lifetime in silicon which, depending on the quality of the crystal, can be in the order of a few nanoseconds to several microseconds. The structure determines the diffusion time of the carriers toward the surfaces, where recombination usually occurs with high rate, and influences the overlap of the carrier distribution with the optical mode. In high repetition rate applications, if the recovery time of the device is longer than the repetition rate of the pulses, the TPA-induced carriers accumulate in the conduction band over many pulses, resulting in increasingly larger loss and optical phase shift that may become data pattern dependent. Therefore, in such applications, it is desirable to engineer devices with a carrier lifetime at least as short as the repetition period. This can be achieved by reverse-biasing a p-i-n structure across a silicon waveguide [35], using porous [36] or poly silicon [37], or by ion-implantation [38–40].

The reduction of carrier lifetime by reverse-biasing the waveguide structure adds complexity to the system and its effectiveness may decrease at high optical intensities [41]. Porous and poly silicon are other options but engineering carrier lifetimes using this method is a complex task. Another method is to introduce defects in the waveguide structures by ion-implantation of different types of ions such as hydrogen, helium, oxygen, or even silicon itself. The operation of this method is based on the principle that a charged particle traveling through matter, releases some of its energy along its path and just before it comes to a stop, it releases most of its energy and creates the most defects. The defects introduced by this process result in the creation of midgap states in the material band structure. These midgap states facilitate the non-radiative recombination of the electrons from the conduction band with holes in the valence band. Therefore, the carrier lifetime can be reduced as a function of the ion-bombardment dose. However, the introduction of these defects in the crystal structure can also result in higher propagation loss along the device. So, a trade-off must be made between the linear loss and the carrier-lifetime as will be demonstrated from the result of this study.

The organization of the paper is as follows. Section 2 consists of a brief description of the devices fabricated for this study. In Section 3, we present a model of pulse-propagation in nonlinear media. This model is utilized to predict the response of silicon waveguides as a function of the input power using the extracted parameters. Section 4 consists of the description of the heterodyne experimental setup utilized in this study. In Section 5, we present the experimental results. We address and propose solutions to several challenges in characterization of nonlinear optical processes in silicon nanowaveguides and present the results of a method to determine input and output coupling losses separately. We utilize the heterodyne pump-probe technique for the direct measurements of all of the nonlinear optical parameters with high sensitivity. In Section 5 also, we further present the results of the effects of proton-bombardment of the silicon nanowaveguides on the carrier recovery time and linear loss.

2. Silicon nanowaveguides

The silicon waveguides studied in the experiments were fabricated using scanning electron-beam lithography (SEBL) as described in [28]. A photograph of one of the chips consisting of several different designs including filters and straight waveguides is shown in Fig. 1(a). Each waveguide structure had multiple bends with straight sections between the bends as illustrated in Fig. 1(b). Different waveguide structures had identical bend sections and straight sections with incremental lengths to enable propagation loss measurements with the cut-off method. These waveguides were fabricated on a silicon substrate consisting of a SiO_2 undercladding and hydrogen silsesquioxane (HSQ) overcladding layers. The waveguides were formed in silicon (n = 3.45), with a height of 106nm and a width of 475nm on a 3μm thick undercladding of SiO_2 (n = 1.45). The structures were overcladded with 1μm of HSQ (n = 1.38) on top of which a 100nm thick layer of SiO_2 was sputtered for protection. The cross-section of the waveguide and the profile of its fundamental TE mode at 1500nm are shown in Fig. 1(c) and Fig. 1(d), respectively.
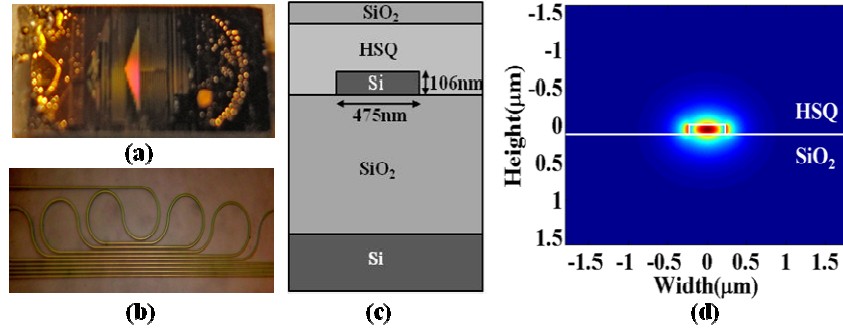
Fig. 1. (a) A photograph of the physical chip on a mount, 1cm in width and about 2.2cm in length. (b) One of the paper clips and bends implemented using high-index contrast (HIC) waveguides. The diameter of each bend is 6μm. (c) Cross-section of the silicon waveguide structure fabricated on silicon substrate with SiO₂ and HSQ cladding layer. (d) The electric field profile of the fundamental TE mode of a high-index contrast silicon waveguide with 106×475nm core.

3. Pulse propagation model

The nonlinear parameter measurements reported in this work were performed using short optical pulses. This section presents a model of short pulse propagation inside a silicon waveguide, which is used to extract the nonlinear parameters from the measurement results. The propagation loss in an optical waveguide is a function of the linear loss, TPA, and FCA. The differential equation describing instantaneous power of an optical pulse as it propagates along the length of a device with linear and nonlinear losses is given by:

$$\frac{dP(z,t)}{dz} = -\left(\alpha_{NL} + \alpha_{lin}\right)P(z,t), \tag{3}$$

where $P(z,t)$ is the instantaneous pulse power in the waveguide, and the losses are divided into linear, α_{lin} and nonlinear α_{NL} components. In this equation, the dispersion broadening can be neglected since the result of cross-correlation of the output pulses show negligible pulse-broadening over a wide range of powers. In addition, the fact that this analysis provides excellent fits to the experimental results as will be demonstrated in Section 5, further supports this assumption. For pulses much shorter than the carrier recovery time, the carrier recombination can be neglected and the nonlinear loss can be modeled by

$$\alpha_{NL}(z,t) = \beta I(z,t) + \sigma \int_{-\infty}^{t} \frac{\beta}{\hbar\omega} I^2(z,t')dt', \tag{4}$$

where β is the TPA coefficient, σ is the FCA effective cross section, $\hbar\omega$ is the energy of a photon, and $I(z,t)$ is the instantaneous intensity of the pulse. The first term in this equation describes the instantaneous loss introduced by TPA which is proportional to the optical intensity. The second term describes absorption due to free-carriers, which accumulates in proportion to the square of the optical intensity and recovers with free carrier lifetime.

The optical mode is highly confined within the waveguide and has a non-negligible longitudinal field component. Since the TPA process is isotropic and depends on the magnitude of the electric fields, to accurately model the TPA loss, the transversal and longitudinal components of the electric field must be accounted for in detail. This is done via a calculation of the effective area as described in [42]. To solve the differential Eq. (3) using a plane-wave approximation for highly confined optical modes, the intensity of the optical signal inside the waveguide must be defined as the ratio of the optical power to an effective area which accounts for the optical mode profile and its interaction with the nonlinear media.

By introducing effective areas, separately for the TPA and FCA processes, Eq. (3) can be written as:

$$\frac{dP(z,t)}{dz} = -\left(\beta \frac{P(z,t)}{A_{TPA}} + \sigma \int_0^t \frac{\beta}{\hbar\omega} \frac{P(z,\tau^{'})}{A_{TPA}} \frac{P(z,\tau^{'})}{A_{FCA}} d\tau^{'} + \alpha_{lin} \right) P(z,t), \qquad (5)$$

where A_{TPA} and A_{FCA}, are defined as the effective areas of the TPA and FCA, respectively. These effective areas are defined so that the intensities

$$TPA : I(z,t) = \frac{P(z,t)}{A_{TPA}} \qquad (6)$$

$$FCA : I(z,t) = \frac{P(z,t)}{A_{FCA}}, \qquad (7)$$

may be defined in terms of a plane-wave mode with the optical power $P(z,t)$ propagating in the optical waveguide. By calculating the overlap of the loss profile as defined by the electric field distribution inside the silicon core with the mode profile, the effective areas are determined. In case of TPA effective area, a rigorous expression was rigorously derived in [42]. However, in case of FCA, a vectorial mode-solver [43] was utilized to find the mode propagation loss numerically given the distribution of loss due to the free carriers across the core. The calculated mode loss was then compared to the plane-wave solution to find the equivalent A_{FCA}. The effective areas, A_{TPA} and A_{FCA} for the silicon waveguides shown in Fig. 1 were determined to be $0.097\mu m^2$ and $0.075\mu m^2$, respectively.

4. Experimental setup

The schematic diagram of the heterodyne pump-probe experimental setup of this study is shown in Fig. 2. The optical source in this experiment consists of a two stage optical parametric oscillator generating 180fs pulses at a repetition rate of 80 MHz and a center wavelength of 1.5μm. The input pulses entering the experimental setup are split into two paths. The splitting ratio is determined using a half-wave plate and a polarizing beamsplitter (PBS). The lower power beam passes through an acousto-optic modulator (AOM) to produce an RF frequency shift of 35MHz. The resulting pulses are used in this experiment as the probe beam. The higher power beam passes through another variable power splitter, where the higher power beam becomes the pump beam and the lower power signal becomes the reference beam. The pump beam is further passed through a variable attenuator and a variable delay stage. The pump and the probe are then combined on a 50:50 splitter with the same polarization. The delay stage in the pump path varies the temporal spacing between the pump and the probe beams.

The combination of the pump and the probe pulses is coupled into a short piece of fiber attached to a 10:90 coupler. The 10% port of the fiber coupler is connected to a power meter to monitor the input optical power. Spliced to the 90% port is a lens-tip fiber. This lens-tip fiber is used to couple the combined pump and probe beams into the waveguide. To optimize the coupling between the fiber and the waveguide, a lens-tip fiber with 1.7μm focal-point beam-diameter was utilized. After traversing the length of the waveguide, pump and probe beams are collected using another 1.7μm lens-tip fiber at the output port. The collected beams are then combined with the reference beam using a fiber-based 50:50 coupler.

The reference beam, prior to being combined with the pump and probe beams is first passed through a separate AOM that shifts its frequency by 36.7MHz. The reference pulses must overlap the probe pulses and arrive at the photodetector at the same time with the same polarization. Therefore, a fixed delay is built into the reference path to ensure this temporal overlap, and a combination of a quarter-wave and a half-wave plate is placed in the reference path for polarization adjustment. The frequency-shifted reference beam thus provides the

heterodyne detection of the probe beam that permits independent measurement of both amplitude and phase changes [34].
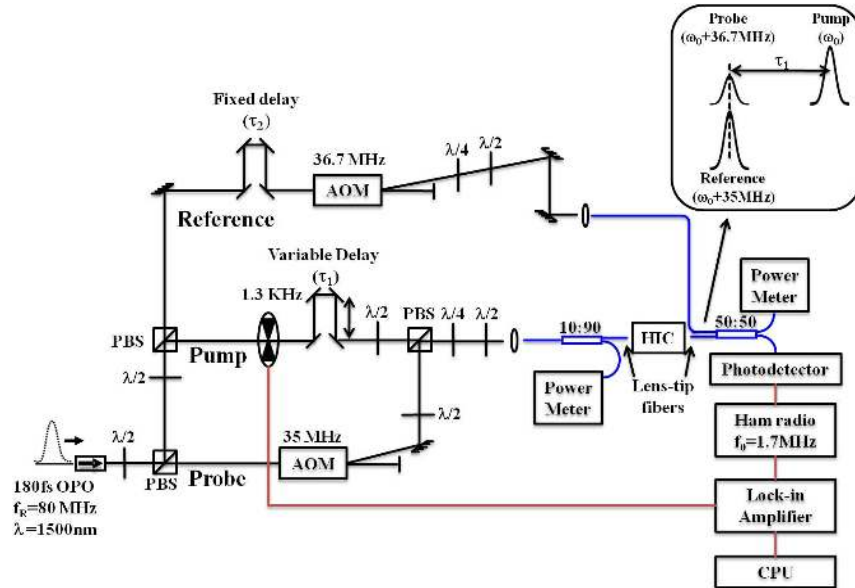

Fig. 2. Schematic diagram of the heterodyne pump-probe experimental setup in this study. The inset shows the relation between the pump, probe, and reference pulses.

As in any pump-probe experiment, the pump beam is chopped at 1.3 KHz to obtain background-free measurements via phase-lock detection.. The interaction of the pump pulses with the waveguide material induces changes in the magnitude and phase of the transmitted probe pulses. The magnitude of the variation is a function of the pump power and the delay between the pump and the probe pulses. The amplitude and phase variation in the probe pulses is translated to phase and amplitude modulation of the heterodyne detection signal.

The AM modulation depth is a function of the absorption induced by the pump, and the FM modulation depth is proportional to the index change induced. The signal is demodulated using an ICOM-IC-R71A Ham radio. The magnitude of the audio output of the radio, in AM or FM mode, is detected using the lock-in amplifier. In the AM mode, the two-photon absorption coefficient and free-carrier induced absorption can be determined, while in the FM mode the Kerr nonlinearity and the free-carrier induced index of refraction change can be characterized.

One of the advantages of utilizing a Ham radio for detection of the AM and FM modulated beat-frequency signal is the narrow-bandwidth of its input filter, resulting in low-noise signal detection. Alternatively, a spectrum analyzer can be used for amplitude detection; however, the filters in a high frequency Ham radio are as narrow as those of the spectrum analyzer, and the radio has the additional capability to detect FM signals. Most importantly, the carrier-phase-lock FM detection by the radio makes phase stabilization of the probe and reference paths unnecessary.

5. Results and discussion

To characterize the ultrafast nonlinear processes in the silicon nanowaveguides, silicon waveguides of different lengths are studied and the results of this study are presented in this section. First, a technique to characterize both the linear loss and optical coupling losses at the input and output ports is discussed. Second, the results of the heterodyne pump-probe experiments characterizing the nonlinear optical losses are presented. Finally, the study of the effects of the proton bombardment on the carrier recovery times and linear optical losses are presented.

5.1 Characterization of linear and coupling losses

To study the nonlinear optical effects in the silicon waveguides, we need to accurately determine the optical power inside the waveguides. Three linear loss mechanisms consisting of linear propagation loss, input coupling loss, and output coupling loss need to be fully characterized. Optical coupling at the input and output ports is achieved using lens-tip fibers. These lensed fibers focus the beam to a 1.7(−0/+0.3)μm beam diameter at their focal planes. The optical coupling loss is dependent on several mechanisms such as the Fresnel reflection at the boundary of air and silicon, mode mismatch between the lens-tip fiber and the waveguide, and the quality of cleaved facets. Due to the variation in the beam waist diameter and variations at the input and output interfaces of the chip, the input and output coupling losses are not necessarily equal; therefore, they need to be accurately characterized individually. For this purpose, we utilize two measurements, the 'cut-back' technique and the nonlinear loss measurement.

Figure 3 demonstrates the various optical loss mechanisms in one of the silicon waveguides.

The total loss can be expressed as:

$$P_{in}(dBm) - P_{out}(dBm) = C_{in} + \left(\alpha_{lin}L + \int \alpha(I)dz\right) + C_{out},$$ (8)

$$C_{in}(dB) = P_{in}(dBm) - P_{iw}(dBm),$$ (9)

$$C_{out}(dB) = P_{ow}(dBm) - P_{out}(dBm),$$ (10)

where P_{in} and P_{out} are the power coupled into the input and output lens-tip fibers, respectively, P_{iw} and P_{ow} are the powers inside the waveguide at the input and output facets, and C_{in} and C_{out} are the coupling losses in dB, α_{lin} is the linear loss in dB/cm, $\alpha(I)$ is the nonlinear loss in dB/cm that varies with intensity of the optical signal inside the waveguide. In Fig. 3, the "input" port is defined to be the port where the pump and probe pulses are coupled into the device, while the "output" port is that end of the device from which the light is collected and directed to the detector.
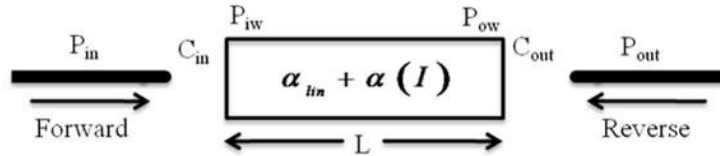

Fig. 3. The notation used for studying waveguide losses, which include input, output, and linear losses. The "input" port is defined to be the port that the pump and probe pulses are coupled into the device. The "output" port is defined to be the port that the light is collected from the device and directed to the photodetector.

Using the cut-back technique, we separate the linear propagation loss from the sum of the input and output coupling losses. This was achieved by coupling light into waveguides of different lengths, measuring the output power as a function of the input power for each case, and plotting the total loss as a function of the device length as shown in Fig. 4. For intensity levels such that the nonlinear effects become negligible (i.e. $\alpha(I)\sim0$), Eq. (8) describes a line with slope α_{lin}, and y-intercept point of $C_{total} = C_{in} + C_{out}$. Linear loss measurements on five waveguides with differential length of 6.1mm between any two adjacent waveguides were conducted. The differential lengths of the waveguide sections were measured using an interferometric technique where the heterodyne pump-probe setup of Fig. 2 was utilized. In this technique, the pump pulse was blocked, while the probe pulse was coupled into waveguides of different length. To obtain an overlap between the probe and reference pulses, the reference arm path length had to be adjusted. The change in the reference path length was

then converted to the path length difference between two adjacent waveguides. Using this data, the total coupling loss of 20.8dB and linear loss of 6.5dB/cm were measured.
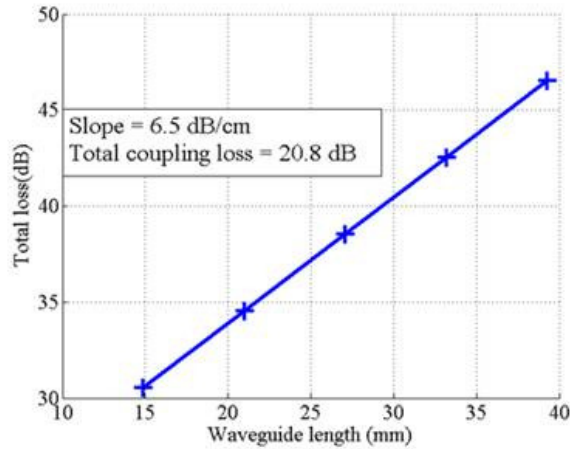

Fig. 4. Total loss as a function of waveguide length. Linear loss of 6.5dB/cm and total coupling loss of 20.8dB were measured.

The intensity-dependent loss as indicated in Eq. (8) results in a deviation of the total propagation loss from the linear case. As the nonlinear term is a function of the intensity of the optical signal coupled into the waveguide, variation in the total loss measured for light coupled in the "forward" and "reverse" directions will indicate the difference between the input and output coupling losses C_{in} and C_{out}. Therefore, the device was tested in both "forward" and "reverse" directions as demonstrated in Fig. 3. The output power collected by the lens-tip fiber as a function of the power put into the input lens-tip fiber was obtained and the results are shown in Fig. 5(a). The black and red curves are obtained in the "forward" and "reverse" directions, respectively. The straight line in this plot corresponds to the linear response, hence any variation from this line is deemed to be the nonlinear loss and is a function of the light intensity inside the waveguide. Higher coupling losses result in lower power inside the waveguide, hence smaller nonlinear optical effects and a roll-off at higher input powers. Any two points on the forward and reverse curves that deviate from the linear response by the same amount correspond to having the same powers inside the waveguide. Therefore, the difference between the forward and backward input powers corresponding to any two such points is equal to the difference between the coupled powers. This is graphically shown in Fig. 5(a) where the two vertical arrows indicate a pair of points with identical nonlinear losses in the forward and reverse directions, and the horizontal arrow indicates the difference between the input powers in the forward and reverse directions indicating the difference between the two coupling losses. The deviation of the output power response from the linear response at the input and output ports is calculated and shown in Fig. 5(b). The difference between the input powers corresponding to the same nonlinear loss is plotted in the inset of Fig. 5(b), and as shown, it is 5.6dB.

The sum and the difference of the input and output coupling losses were determined to be 20.8dB and 5.6dB, respectively. These two sets of data lead to each input and output coupling losses C_{in} = 13.2dB and C_{out} = 7.6dB. The large difference between the input and output coupling losses emphasizes the importance of a careful characterization. This difference is due to fabrication tolerances, both for the curvature of the lensed-tip fiber, as well as the uniformity of the cleave quality of the silicon chip facets.
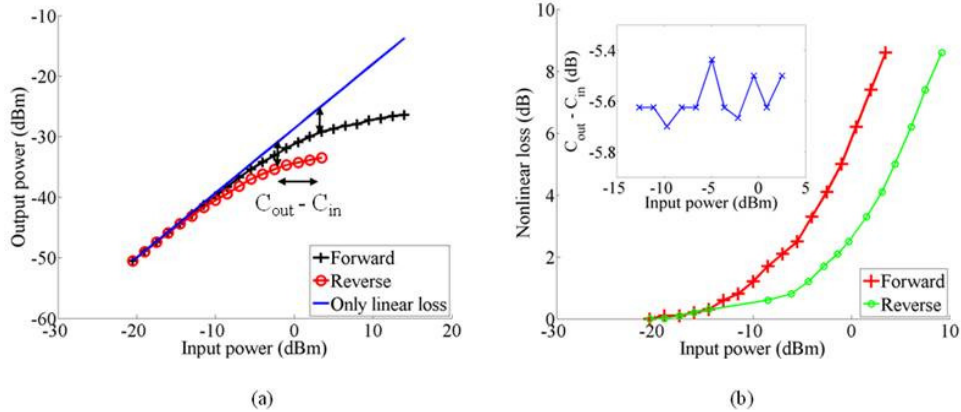
Fig. 5. (a) Response of the silicon waveguide when the light is coupled in the forward and then in the backward directions as a function of the average power, with the source as described in Section 4. The straight line corresponds to the linear response with no nonlinearities. (b) Nonlinear loss in the forward and reverse direction as a function of the input power, and the difference between the two coupling losses, resulting in 5.6dB loss difference (inset).

5.2 TPA and FCA magnitudes

The heterodyne pump-probe method, as described in Section 4 was used to study both the instantaneous and longer-lived nonlinearities enabling high sensitivity and simultaneous characterization of both amplitude and phase response of a device. Figure 6(a) shows the normalized measured change in the probe signal amplitude as a function of the delay of the probe with respect to the pump. Figure 6(b) shows the amplitudes of the instantaneous and slow-recovery loss as a function of the input pulse energy. The ultrafast carrier dynamics in the silicon devices as demonstrated in this figure consist of two distinct processes, an instantaneous component at time delay ($\tau_1 = 0$), followed by a slow recovery time of several hundreds of picoseconds. The amplitude of the instantaneous component is proportional to the intensity of the light inside the waveguide and is caused by two-photon absorption, while the magnitude of the longer-lived response is due to absorption of the probe pulse by the free carriers generated in the TPA process.
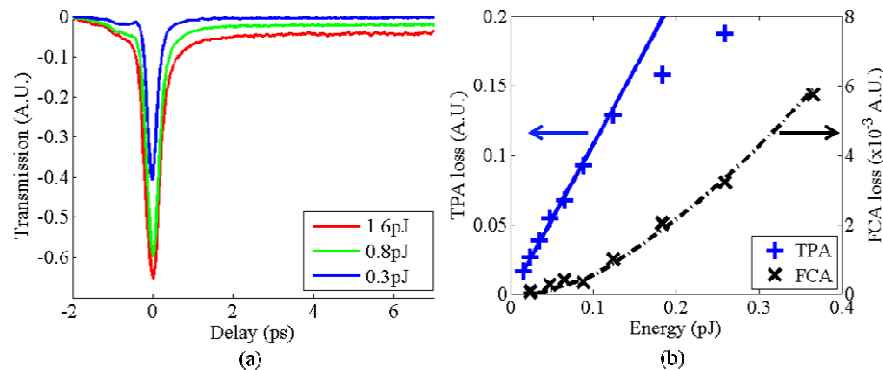

Fig. 6. (a) Change in the magnitude of the probe signal transmission as a function of delay between the pump and probe signals for pump pulse energies shown in the legend. (b) The magnitude of the TPA and FCA loss as a function of input pulse energy extracted from the pump-probe traces is shown. The measured and calculated total loss due to TPA and FCA in a silicon waveguide with cross section of 106nm × 475nm and length of 14.9mm are shown. The TPA loss is shown with (+) markers and the slope of the linear line indicates the TPA coefficient. The measured FCA loss is shown with (+) markers, and the quadratic fit was achieved using the calculated carrier density in the device with FCA effective cross section of $1.9 \times 10^{-17} \text{cm}^2$.

The FCA loss was derived from the pump-probe measurement at 5ps time delay, and the TPA loss was then determined by fitting the $\tau=0$ response including the initial fast rise of FCA consistent with Eq. (13). The measured amplitudes of the instantaneous TPA-induced loss and long-lived FCA loss are shown in Fig. 6(b). The TPA loss is shown in blue and consists of a linear section at lower pulse energy levels, while at higher input energy levels the magnitude of this loss saturates as the pump pulse begins to experience loss through its own TPA. The linear section of the curve is dominated by the TPA effect which is proportional to the intensity and the TPA coefficient (β). The instantaneous response due to TPA at low input pulse energy levels can be described by the following equation

$$\frac{dI_s}{dz} = -\left(\beta I_p + \alpha_{lin}\right)I_s,\tag{11}$$

where I_p and I_s are the pump and probe intensities inside the waveguide, respectively. Integrating this equation and solving for a change in I_s due to I_p, we have

$$\frac{\Delta I_s}{I_s} = \beta I_p \left(\frac{1-e^{-\alpha_{lin}L}}{\alpha_{lin}}\right) = \beta I_p L_{eff},\tag{12}$$

where the new variable L_{eff}, the effective length of the device, is a function of physical length L, and the linear loss α_{lin}, and I_p is the pump intensity defined as the ratio of the pump power to the TPA effective area. For long waveguides, the effective length reduces to $1/\alpha_{lin}$. The silicon waveguides in this study had a dimension of 106nm × 475nm and length equal to 14.9mm. $A_{TPA,eff}$ was calculated via an overlap integral of E-field and the nonlinear medium [42], to be 0.098μm^2 and L_{eff} was found to be 6mm. From the slope of the TPA loss as shown in Fig. 6(b), we extract the TPA coefficient to be 0.68 cm/GW. This compares with the mid range of values previously published [9].

Each pair of photons absorbed as a result of the TPA process, generates an electron-hole pair. Both the electrons in the conduction band and the holes in the valence band in turn absorb photons and result in further optical loss. The total absorption due to FCA in a waveguide of length L is a function of the number of free-carrier pairs and is described by:

$$\alpha_{T,FCA} = \int_0^L \sigma N dz = \sigma \int_0^L dz \int_{-\infty}^{t} \frac{\beta I^2\left(z,t'\right)}{\hbar\omega} dt' = \sigma \frac{N_{total}}{A_{FCA}},\tag{13}$$

where $\alpha_{T,FCA}$ is the total loss due to free-carrier absorption, N is the density of carrier pairs per cm^3, and N_{total} is the total number of carrier pairs generated. The intensity in this case is calculated by taking into account two effective areas, as in Eq. (5).

$$I^2\left(z,t\right) = \frac{P\left(z,t\right)}{A_{TPA}}\frac{P\left(z,t\right)}{A_{FCA}}.\tag{14}$$

The total FCA loss is proportional to the total number of carriers generated which is in turn a function of the square of the optical intensity. To calculate the FCA effective cross-section, first, we need to calculate the number of carriers in the waveguide as a function of the input pulse energy. Referring back to Eq. (11), we can see that in the absence of any nonlinearity, the optical output power of the device is a linear function of the input power. Therefore, any deviation from a linear response is due to the TPA and FCA processes. To calculate the number of TPA-induced free-carriers, the output pulse energy of the device as a function of the input pulse energy is measured. The direct input versus output energy measurement was performed by direct detection of the output power using a power meter, and by chopping the input signal and detecting the modulated output signal at the chopped frequency using a lock-in amplifier. The result is shown in Fig. 7.

The densities of the electrons and holes generated by TPA are equal. Thus, in the range that FCA is negligible,

$$N_{Total,e} = N_{Total,h} = \frac{\Delta E}{2\hbar\omega}\left(\frac{1 - e^{-2\alpha_{lin}L}}{1 - e^{-\alpha_{lin}L}}\right)\frac{e^{\alpha_{lin}L}}{2}, \qquad (15)$$

where ΔE is the deviation of the output energy due to nonlinearity as demonstrated in Fig. 7, $\hbar\omega$ is the energy of the photons, α_{lin} is the linear loss, and L is the physical length of the device. The result of the calculation using Eq. (15) is shown in Fig. 9 with (+) markers, which demonstrates a quadratic dependence on the input pulse energy.
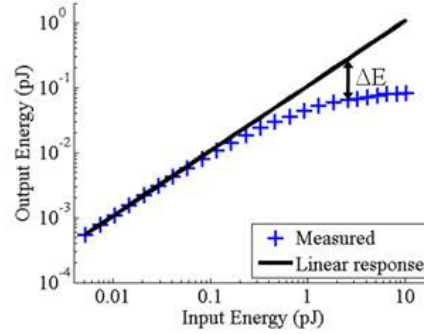

Fig. 7. Measured (+) output energy as a function of the input power in the silicon waveguide of length 1.49cm. The linear response is also plotted. ΔE demonstrates the loss due to the nonlinearity in the device.

The carriers generated by this process diffuse at the rate of 36cm^2/sec [44] and redistribute evenly across the waveguide cross within a few picoseconds. Therefore, an effective area for the overlap of the E-field of the propagating mode with this rectangular cross section is calculated and is equal to 0.075μm^2. In the regime that linear loss still dominates over nonlinear loss, these carriers are distributed along the length of the device over the FCA effective length, $L_{FCA,eff}$ given by:

$$L_{FCA,eff} = \frac{1 - \exp(-2\alpha_{lin}L)}{2\alpha_{lin}}. \qquad (16)$$

where the factor of two in the denominator is due to the dependence of free-carrier density on the square of the optical intensity. The total FCA loss is determined from the heterodyne pump-probe experimental results by measuring the transmission loss at time delays larger than 5ps, which is approximately how long it takes for the carriers to diffuse to a uniform transverse distribution. The magnitude of this loss as a function of the input pulse energy is calculated from the pump-probe traces of Fig. 6(a), and shown in Fig. 6(b). The fit to the measured data is accomplished using the carrier density calculated using Eq. (13) and Eq. (15) with the FCA effective cross section $\sigma = 1.9 \times 10^{-17}$ cm^2. The summary of the extracted parameters described in this section is given in Table 1.

Table 1. The extracted parameters of the imaginary part of the refractive index at 1500nm

Parameter	Value
TPA coefficient (β)	0.68 (cm/GW)
FCA effective cross section (σ)	1.9 x 10^{-17} (cm^2)
Linear loss (α_{lin})	1.50 (cm^{-1})

5.3 Comparison of simulation and experimental results

To further verify the linear and nonlinear parameters extracted thus far, the differential equation describing the pulse evolution along the length of the device, as given by Eq. (5) was solved numerically using the parameters given in Table 1. The output pulse energy of the

device as a function of the input pulse energy was predicted and compared to the direct input vs output energy measurement described in the previous section. The result is shown in Fig. 8. The solid line is the simulation result while the measured data are shown with (+) markers. The results show an excellent agreement between the model and the measured data.
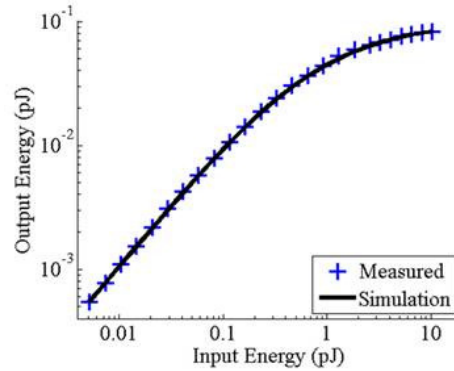

Fig. 8. Output pulse energy as a function of the input pulse energy of the 14.9mm long silicon waveguide. The simulation was performed using $\beta = 0.68$ cm/GW and $\sigma = 1.9\text{x}10^{-17}$ cm^2, $\alpha_{lin} = 150$ cm^{-1}, $\tau = 180$fs, $\lambda = 1500$nm, repetition rate = 80MHz.

Using this simulation technique, we can also calculate the carrier density inside the waveguide as a function of the length of the device. This calculation can be performed by keeping track of the amount of light absorbed by the TPA process resulting in:

$$N_{Total,e} = N_{Total,h} = \int_0^L N(z) A_{FCA} dz = \int_0^L \int_0^t \frac{\beta}{\hbar\omega} \frac{P(z,\tau')}{A_{TPA}} \frac{P(z,\tau')}{A_{FCA}} d\tau' A_{FCA} dz. \quad (17)$$

The total number of carriers as a function of the input optical energy calculated with this approach is shown in Fig. 9, and is compared to that obtained from the fit to output response of the device shown in Fig. 7. It is evident from Fig. 9 that the simulated total number of carriers agrees very closely with the measured results indicating the validity of the models used to describe nonlinear pulse propagation.
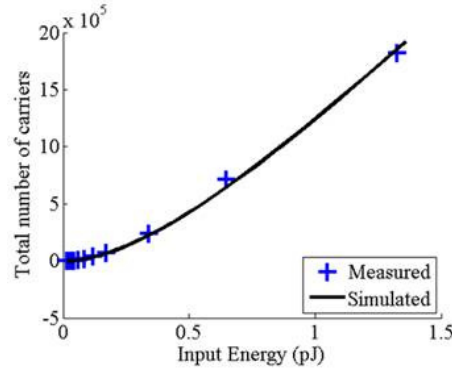

Fig. 9. Total number of TPA-generated carriers in the waveguide as a function of the input pulse energy. (+) data is calculated based on direct measurement of the output pulse energy vs input pulse energy. The solid black line is the result obtained from numerically simulating the pulse propagation along the device.

5.4 Optical Kerr effect and free-carrier index changes

Figure 10(a) shows the normalized heterodyne pump-probe traces using FM detection. In this figure, the horizontal axis indicates the delay between the pump and probe pulses, and the

vertical axis is the measured phase change incurred by the probe signal. As demonstrated in this figure, the pump-probe response consists of an instantaneous response at time delay of zero which is linearly dependent on the pulse intensity. The instantaneous response is attributed to the phase response incurred by the probe due to Kerr nonlinearity. This instantaneous component is followed by a slow recovery response of several hundreds of picoseconds. The change in sign is due to the opposite signs in the induced refractive index changes for Kerr nonlinearity and for TPA-induced free carriers. The magnitude of the phase change is a function of the number of generated free-carriers, hence proportional to the pump power squared. To detect this optical phase change, the FM modulation using the Ham radio as described in Section 4 is used. A major advantage of the FM radio is that it automatically tracks and locks onto the RF carrier and thus, circumvents the need to interferometrically stabilize the optical phase between probe and reference.
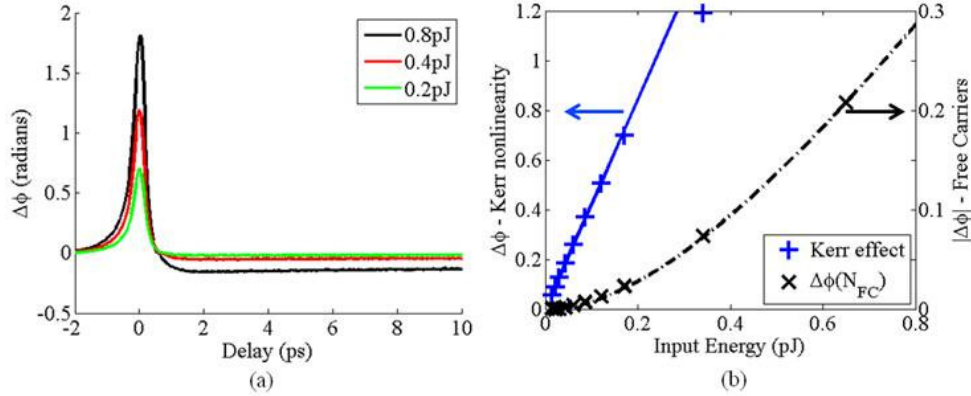

Fig. 10. (a) Measured probe phase change as a function of the delay between the pump and probe pulses for pump pulse energies indicated in the legend. (b) Optical Kerr effect and free-carrier induced phase change as a function of optical energy. n_2 is calculated to be 3.2×10^{-14} cm^2/W. $|\Delta\phi|$ induced as a function of free-carrier density vs energy is shown on the right axis. The fit is achieved using $\xi = -5.5 \times 10^{-21}$ cm^3.

In the same manner used to separate the nonlinear loss components, the free-carrier index changes were determined from the pump-probe traces at 5ps time delay and the instantaneous Kerr coefficient was obtained from the fit at $\tau = 0$ that also took into account the fast rise of the free-carriers. From these measurements, we can determine both the Kerr nonlinearity and refractive index change as a function of carrier density for these high index-contrast silicon waveguides. As with the TPA characterization of the previous section, the magnitude of the induced phase change at zero time delay ($\tau_1 = 0$) can be related to optical energy inside the waveguide. These results are shown in Fig. 10(b). The measurement consists of a linear region at pulse energies of up to 20pJ beyond which the maximum phase change starts to deviate from the linear line due to the pump depletion. The Kerr coefficient can be determined from:

$$\Delta n = \frac{\lambda}{2\pi L_{eff}} \Delta f = n_2 I, \qquad (18)$$

where Δn is the change in the refractive index due to the Kerr effect, λ is the wavelength of the optical signal, L_{eff} is the effective length of the device as defined in pervious section, $\Delta\phi$ is the induced phase change, I is the intensity of the optical signal inside the waveguide, and n_2 is the Kerr coefficient. The effective length and effective area for Kerr nonlinearity are defined as for the TPA measurement. From the slope of the linear portion of the optical Kerr nonlinearity plot shown in Fig. 10(b), we extracted the Kerr coefficient to be $n_2 = 3.2 \times 10^{-14}$

cm^2/W. This value is in close agreement with the previously published data using z-scan technique as tabulated in [9].

In addition to the instantaneous response, we can observe an induced phase change after a 5ps delay which has a long recovery time. This induced phase change, similar to the induced FCA loss, is a function of the number of free carriers generated by the TPA process. Therefore, we can take advantage of the earlier calculations of the number of carriers to determine the index of refraction change as a function of the carrier density.

As discussed, the free-carriers are distributed uniformly over the cross-section of the waveguide and can be treated as uniform over the effective length, $L_{FCA,eff}$ as well. Using the total number of carriers, we define the refractive index change as a function of carrier density as:

$$\Delta n_{FCA} = \xi \frac{N_{total}}{A_{FCA} L_{FCA,eff}}, \tag{19}$$

where Δn_{FCA} is the total change in the refractive index due to free-carriers, ξ is a proportionality constant, N_{total} is the total number of carrier pairs generated over the waveguide length [30]. The fit as shown in Fig. 10(b) was achieved using $\xi = -5.5 \times 10^{-21}$ cm^3. The results obtained in this section are summarized in Table 2.

Table 2. Kerr Coefficient and Refractive Index Change Due to Free Carriers

Parameter	Value
Kerr coefficient (n_2)	3.2x10^{-14} (cm^2/GW)
Refractive index change per carrier per unit volume(ξ)	-5.5x 10^{-21} (cm^3)
Wavelength (λ)	1.5 (μm)

5.5 Carrier recovery time and proton bombardment

In addition to the optical nonlinear processes discussed up to this point, the carrier recovery time in the silicon waveguides will dictate their usefulness in high speed optical systems. It has been shown that active carrier sweep-out with p-i-n structures can yield a shorter lifetime results than proton bombardment technique, but at the expense of the energy needed to extract the carriers [35]. Therefore, in this section, a study of the effects of ion implantation on the carrier recovery time and linear loss of the silicon samples is presented. Proton bombardment of samples results in creation of defects in the crystal structure [45, 46]. These defects create midgap states which speed up the recovery time of the device. It has been shown that while higher doses of ion implants result in greater reduction of the carrier recovery time, these defects result in higher scattering and absorption through the device.

For the purpose of this study, several silicon waveguide chips were ion implanted at dosages varying from 10^{12} to 10^{15} /cm^2. It was necessary to determine the energy level of protons that would penetrate different layers of the structure. These layers are illustrated in Fig. 1(c). In order for the protons to reach the silicon waveguides, they must penetrate through 100nm layer of SiO$_2$, 1μm of HSQ, and get implanted in the 100nm-thick silicon waveguide. To determine the proper energy levels, the SRIM program was utilized (www.srim.org). Based on Monte-Carlo analysis, the SRIM program simulates the penetration depth of protons of different energy accounting for scattering, energy loss, and non-uniformity of proton energy levels. Each device was proton-bombarded using a combination of three different proton energies of 80, 90, and 100KeV to account for variations in the density of HSQ layer, which is highly dependent on the fabrication process, and to still create the desired distribution of defect states in the silicon waveguides. As shown in Fig. 1(c), the silicon waveguides start at the depth of 1100nm and extend to 1206nm where the largest number of defect states is created.

After proton-bombardment of the samples, their linear loss and recovery times were measured and plotted in Fig. 11. A recovery time as short as 33ps for a linear loss of only 14.8dB/cm was obtained at the highest proton-bombardment level of 10^{15}/cm^2. This

combination of recovery time reduction and degradation in linear loss seems to be the best thus far reported for the proton bombardment technique [39].
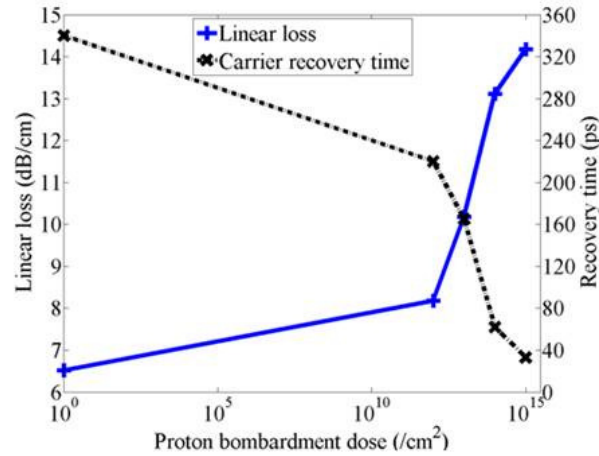

Fig. 11. Linear loss and carrier recovery time as a function of the proton bombardment.

6. Conclusion

In this paper, the ultrafast nonlinear optical properties of high-index contrast silicon waveguides of 106nm×475nm cross-section were studied. Input and output optical coupling was accomplished using lens-tip fibers, and both cut-back to determine propagation loss and forward-backward nonlinear measurements were used to determine individual coupling losses. A measured 5.6 dB difference between the coupling efficiencies at the input and output ports demonstrated the importance of such measurement to determine the internal optical pulse energy accurately. The heterodyne pump-probe technique was utilized to characterize the magnitude of the TPA and FCA losses as well as the Kerr nonlinearity and the refractive index change as a function of the carrier density. The high sensitivity of the heterodyne technique has allowed for this characterization with only relatively small induced carrier densities. The two-photon absorption coefficient and free-carrier absorption effective cross-section were determined to be 0.68cm/GW, and 1.9×10^{-17} cm^2, respectively and the Kerr coefficient and free-carrier-induced refractive index change 0.32×10^{-13} cm^2/W, and -5.5×10^{-21} cm^3, respectively. The parameters extracted were applied to a model predicting the output power response of the waveguides as a function of the input power. This model was utilized to predict the limitations imposed by the nonlinearity on the transmission of pulsewidths of different duration [47]. As the carrier recovery of silicon can be in the order of several hundreds of picoseconds to nanoseconds, the devices were proton bombarded with different doses to determine the relationship between reduced lifetime and induced additional loss. Carrier lifetime of 33ps with proton bombardment level of 10^{15} /cm^2 with an increase of linear loss to 14.8dB/cm was achieved.

Acknowledgments